Exploring the Role of Deep Moist Convection in the Wavenumber Spectra of Atmospheric Kinetic Energy and Brightness Temperature

DA FAN,[a,b] STEVEN J. GREYBUSH,[a,b] XINGCHAO CHEN,[a,b] YINGHUI LU,[a,b] FUQING ZHANG,[a,b] AND GEORGE S. YOUNG[a,b]

[a] *Department of Meteorology and Atmospheric Science, The Pennsylvania State University, University Park, Pennsylvania*
[b] *Center for Advanced Data Assimilation and Predictability Techniques, The Pennsylvania State University, University Park, Pennsylvania*

(Manuscript received 26 October 2021, in final form 8 July 2022)

ABSTRACT: Through a series of global convection-permitting simulations and geostationary satellite observations, this study investigates the role of deep moist convection in atmospheric kinetic energy (KE) and brightness temperature (BT) spectra in a realistic framework. The control simulation was produced on a quasi-uniform 3-km global mesh, which allowed the explicit representation of deep convection. To assess the impact of deep moist convection, a fake-dry simulation was performed with latent heating–cooling feedback in the microphysics removed for comparison. The impacts of deep moist convection on mesoscale KE spectrum are concentrated on energizing the mesoscale at the upper troposphere and the lower stratosphere through buoyancy production. BT spectra for the control simulation have a similar shallow slope in the mesoscale as that for the observations. The greater spectral power of BT for the control simulation compared to the observed is attributed to the dislocation and higher intensity of simulated convection. The observed BT spectra exhibit a large diurnal variability due to the diurnal variation of the intensity of convection. The simulated BT spectrum is dependent on convective systems at different scales. Deep convection in the intertropical convergence zone (ITCZ) and shallow convection in the North Pacific storm-track region play an important role in energizing the convective scale of the BT spectrum. In the mesoscale, the BT spectrum is mainly energized by mesoscale convective systems (MCSs) in the ITCZ. Tropical equatorial waves and baroclinic waves in the southern midlatitudes are critical in producing the shallow slope near −5/3 and providing energy in the BT spectrum at the synoptic scale.

SIGNIFICANCE STATEMENT: We further explore the role of deep moist convection in kinetic energy and brightness temperature spectra through high-resolution radiance observations and convection-permitting simulations. Moist processes can energize the mesoscale of kinetic energy. Brightness temperature spectra show dependence on convective systems at different scales. These results point the way toward a new approach to evaluate the predictability of convective systems, and future development of model dynamics and parameterization.

KEYWORDS: Deep convection; Infrared radiation; Cumulus clouds; Model evaluation/performance; Numerical weather prediction/forecasting

1. Introduction

The kinetic energy (KE) spectrum has been found to be an important tool in investigating atmospheric predictability since the 1960s. Lorenz (1969), who employed a spectral turbulence model as an idealized atmospheric model, demonstrated that the predictability of atmospheric models depends on the logarithmic slope of the flow's KE spectrum. Long-range aircraft measurements in the 1970s suggested a canonical structure of atmospheric KE spectrum following a power law close to a slope of −3 at the synoptic scale (500–2000 km) with a transition to −5/3 power law at the mesoscale (<500 km) (Nastrom and Gage 1985; Lindborg 1999). Similar KE spectra can also be computed from global and regional numerical weather prediction (NWP) model simulations (e.g., Skamarock et al. 2014; Durran and Gingrich 2014; Selz and Craig 2015; Sun et al. 2017; Durran and Weyn 2016; Judt 2020). The ability of an atmospheric model to reproduce the canonical KE spectrum is often considered as a way to validate the model's configuration and formulation (Skamarock 2004; Skamarock et al. 2014). The dynamics underlying the atmospheric energy spectrum is critical to atmospheric predictability across scales, but is still not well understood. This study is intended to address this issue by exploring the role of deep moist convection in atmospheric kinetic energy and brightness temperature spectra in the context of global high-resolution nonhydrostatic simulations and high-resolution geostationary satellite infrared radiance observations.

The role of moist convection in mesoscale KE spectrum has been explored in many studies using idealized and full-physics simulations (e.g., Hamilton et al. 2008; Durran and Weyn 2016; Waite and Snyder 2013; Sun and Zhang 2016). Hamilton et al. (2008) compared mesoscale KE spectra in global simulations with and without moisture, and found that moist processes can energize the mesoscale. Durran and Weyn (2016) showed that idealized squall lines alone, growing in an environment without any background KE, were able to generate the −5/3 energy spectrum at wavelengths less than 400 km.

Zhang: Deceased.

Corresponding author: Da Fan, dxf424@psu.edu

DOI: 10.1175/JAS-D-21-0285.1

Sun and Zhang (2016) confirmed the findings of Durran and Weyn (2016), and further exhibited that moist convection plays a critical role in producing the −5/3 slope in the mesoscale KE spectrum through the comparison between idealized dry and moist baroclinic waves. Moist processes are also found important in the error energy propagation (Zhang et al. 2003, 2007; Selz and Craig 2015; Judt 2020). Thus understanding the role of moist convection in KE spectrum might also be critical for predictability studies.

Satellite infrared brightness temperature (BT) observations have been used as a proxy for moist convection, but its power spectrum has only received limited attention. Recently, Shamir et al. (2021, their Fig. 1) found that wavenumber-frequency spectra of tropical BT using satellite observation can well capture the features of equatorial waves predicted by Matsuno (1966). Chan et al. (2020, their Fig. 5) found that both observed and simulated infrared BT power spectra have a spectral slope of −5/3 in the mesoscale. The −5/3 power law is usually associated with an energy cascade in isotropic turbulence (Tennekes and Lumley 1972), and thus the similar behavior in the BT spectrum is worth further investigation. The dynamics behind the BT spectrum across scales is first explored in this study.

In this study, we employ the state-of-the-art operational NWP model used by the U.S. National Oceanic and Atmospheric Administration (NOAA), the Geophysical Fluid Dynamics Laboratory (GFDL) finite-volume-cubed-sphere dynamical core (FV3) with Global Forecast System (GFS) physics (fvGFS) modeling system (Zhou et al. 2019; Hazelton et al. 2018; J.-H Chen et al. 2018) to perform global high-resolution simulations at mean mesh spacings of 3–13 km. We also use high-spatiotemporal resolution infrared radiance observations from the newly developed geostationary weather satellite, *GOES-16*. Most analysis is based on the 3-km control simulations because they explicitly allow convection. The purpose of this study is to explore the role of convection in atmospheric KE spectra and BT spectra by connecting FV3 simulations with *GOES-16* observations. Specifically, the goals are to 1) investigate the role of deep moist convection in mesoscale −5/3 KE spectra, 2) explore the role of deep moist convection in BT spectra, and 3) examine the dependence of the BT spectrum on convective systems across scales.

This paper is structured as follows: section 2 introduces the model configuration and observation data. Section 3 introduces two spectral analysis methods: spherical harmonic transform and continuous wavelet transform. Section 4 explores the role of convective systems in KE and BT spectra, the dependence of BT spectra on convective systems, and the sensitivity of KE and BT spectra to the deep convection parameterization. The paper concludes with a summary in section 5.

2. Data

a. FV3 model configuration

The primary data source for this study is a series of global convection-permitting numerical weather prediction (NWP) model (GCPM) simulations produced with the GFDL FV3. In 2016, the FV3, developed at the NOAA/GFDL, was selected as the dynamic core of the Next Generation Global Prediction System (NGGPS) to replace Global Spectral Model (GSM). FV3 was chosen for its accuracy, adaptability, and computational efficiency, which brings a great opportunity for the unification of weather and climate prediction systems. During NGGPS Phase II, a new model using the FV3 nonhydrostatic dynamic core coupled to the physics package from NCEP/GFS was built at GFDL, called fvGFS. The nonhydrostatic dynamics in the FV3 allows the fvGFS to run globally at resolutions high enough to explicitly simulate convective-scale motions (Lin 2018). Compared to the old-generation GFS, the 13-km fvGFS outperforms in tropical cyclone intensity prediction for all basins (Chen et al. 2019).

TABLE 1. List of choices of convection parameterizations for each simulation.

Name	Grid spacing (km)	Convection parameterization	Latent heating–cooling in the microphysics
3 km (control)	3	No	Yes
3 km (fake-dry)	3	No	No
6 km	6	Yes	Yes
6 km (no cp)	6	No	Yes
13 km	13	Yes	Yes
13 km (no cp)	13	No	Yes

In this study, we used the global quasi-uniform 3-km fvGFS configuration with deep convective parameterization scheme switched off as the control simulations, which is consistent with the configuration in Zhang et al. (2019). The model has 63 vertical layers with the model top at 0.64 hPa. The radiation scheme is the Rapid Transfer Model for GCMs (RRTMG; Iacono et al. 2008). The boundary layer scheme is the Yonsei University (YSU) PBL scheme based on Han and Pan (2011). The GFS scheme (based on Zhao and Carr 1997) has been replaced by the GFDL cloud microphysics scheme (Chen and Lin 2013). The horizontal advection scheme is the unlimited "fifth-order" scheme with weak 2Δ filter. To explore the role of deep moist convection in the KE and the BT spectrum, a 3-km "fake-dry" simulation (Melhauser and Zhang 2012) was performed with the latent heating-cooling feedback turned off in the microphysics for the full simulation period. To investigate the sensitivity to the convective parameterizations and horizontal resolutions, we also performed sensitivity experiments using 6- and 13-km mesh with and without the deep convection scheme. In the experiments with deep convection scheme, the model employs the scale-aware version of the simplified Arakawa–Schubert (SAS) cumulus parameterization scheme (Arakawa and Schubert 1974; Han et al. 2017). Details of convection parameterization scheme and resolution for each simulation are listed in Table 1. A 13-km mesh is also employed in the current operational GFS and its performance is examined in this study.

The simulation results in this study were computed from a 3-day simulation initialized from 1200 UTC 24 August 2017. It should be also noted that the first 24 simulation hours were not included in the computation to avoid any spinup issues. The spinup issue is further investigated in section 4a.

To generate BT from FV3 simulations, we employed the Community Radiative Transfer Model (CRTM; Han et al. 2006, 2007), version 2.3.0, to translate model state variables into simulated radiances. CRTM is a rapid forward model to calculate BT with the Successive Order of Interaction (SOI) forward solver (Heidinger et al. 2006). To calculate the BT over the globe, the sensor zenith angle in CRTM is set to 0°. The possible impacts of the universal sensor zenith angle will be discussed in section 5.

b. GOES-16 *observations*

Satellite observations of interest for this study are the infrared BTs (also referred to as radiances) from *GOES-16*. *GOES-16* was launched in November 2016 and provides 6 visible and 10 infrared channels of all-sky BT using its Advanced Baseline Imager (ABI) with 1–2-km horizontal resolution available every 15 min under the routine surveillance mode (Schmit et al. 2017). The infrared BTs in channel 8 (wavelength is 6.2 μm) and 10 (wavelength is 7.3 μm) are sensitive to upper-troposphere and lower-troposphere atmospheric water vapor content in clear-sky regions, with peak weighting functions of ~344 and ~618 hPa assuming a standard atmosphere (Schmit et al. 2017) which can vary considerably depending on the water vapor profile. In our study, hourly *GOES-16* BTs from channels 8 and 10 were selected to perform spectral analysis over the same time period as that for FV3 simulations. In cloudy regions, both channels sense the top of the cloud layer, with colder BTs being associated with deeper clouds (Jones et al. 2020). Therefore, infrared BTs can well represent the intensity, distribution, and structure of convection and convective systems. The observed BTs from 1200 UTC 25 August to 1200 UTC 27 August 2017 were selected for comparison.

3. Methods

a. *Spherical harmonic transform*

Spherical harmonic transform (SHT) was proven to be fast and accurate for performing global spectral analysis (Skamarock et al. 2014). In this paper, SHT was performed on KE field from FV3 simulations, as well as BT fields from both FV3 and *GOES-16* to calculate one-dimensional (1D) power spectrum. 1D power spectra represent the distribution of energy across scales.

Since the gnomonic grid in the FV3 model and the "ABI fixed grid" of *GOES-16* do not directly lend themselves to the computation of KE spectra, we interpolated the FV3 and *GOES-16* fields from their native meshes to a uniform latitude-longitude mesh with the same mean grid spacing as the FV3 and *GOES-16* over the globe using linear interpolation. Since the coverage area of *GOES-16* is only about 1/3 of Earth's surface, BTs in the "well-observed" region with the sensor zenith angle less than 60° were extracted from *GOES-16* observations. The deviation of BTs in the region of interest was calculated by subtracting the mean BT in the region from the BT, while BT in the remainder of the area were zero padded. The deviation of BT over the globe can be expressed by

$$\mathrm{BT}' = \begin{cases} \mathrm{BT} - \overline{\mathrm{BT}}, & \Theta \le 60°, \\ 0, & \Theta > 60°, \end{cases} \tag{1}$$

where BT′ is the deviation of BT, $\overline{\mathrm{BT}}$ is the mean BT in the well-observed region, and Θ is the sensor zenith angle. The deviation of BT was applied to compute the observed BT spectra. The regional FV3 BT spectra were also computed in the same way and over the same region. The spectra of padded BT from *GOES-16* and FV3 simulations will be compared in section 4b, while the spectra of unpadded BT for FV3 simulations will be discussed in section 4c. A SHT was employed to these interpolated latitude–longitude fields. All resulting two-dimensional (2D) wavenumber decompositions were summed over spherical harmonics with the same total wavenumber to produce a 1D spectrum. As given in Cavanaugh et al. (2017), a 1D spectrum $E_f(l)$ can be constructed as a function of spherical wavenumber l such that

$$E_f(l) = \sum_{m=-l}^{l} c_{lm} |f_{lm}|^2, \tag{2}$$

where c_{lm} is a normalizing constant. In this study, f_{lm} is the spectral coefficient matrix of BT and horizontal winds fields; and l and m are the zonal and meridional wavenumber, respectively. Since the vertical transfer of KE is not the focus of our study, the KE spectrum, $\mathrm{KE}_f(l)$, is constructed through the spectral coefficients of horizontal winds u and v without considering the vertical change of density such that

$$\mathrm{KE}(l) = \frac{1}{2} \sum_{m=-l}^{l} (c_{lm} |u_{lm}|^2 + c'_{lm} |v_{lm}|^2), \tag{3}$$

where u_{lm} and v_{lm} are the spectral coefficients of horizontal winds, respectively. The mean KE and BT spectra were computed by taking the 1D spectrum at each hour, and averaging the spectrum over 24 h to remove the diurnal variation. To explore the role of dynamics producing KE spectra, the spherical harmonics representation of the horizontal wind was decomposed into a divergent and a rotational component.

We present constant pressure KE spectra and their divergent and rotational component at three different characteristic levels: 100, 300, and 700 hPa. The characteristics of KE in the troposphere are analyzed through the spectra of KE on 300 and 700 hPa surface, while those for lower stratosphere are explore through the spectra of KE on 100 hPa, which is near the tropopause in the tropics.

b. *The two-dimensional continuous wavelet transform*

Two-dimensional (2D) continuous wavelet transform (CWT) can produce localized spectral information of the underlying dataset. Compared to traditional spectral analyses like SHT and Fourier transform, 2D CWT can provide detailed spatial distribution of localized spectral power for different scales about meteorological fields. The 2D CWT is a convolution in the space ($\mathbf{x}$) domain between a 2D signal $f(\mathbf{x})$, and the mother wavelet $\psi(\mathbf{x})$, yielding wavelet coefficient, $g(s, \mathbf{t}, \alpha)$. The wavelet coefficient $g(s, \mathbf{t}, \alpha)$ at scale s, location $\mathbf{x}$, and a given orientation α is given by

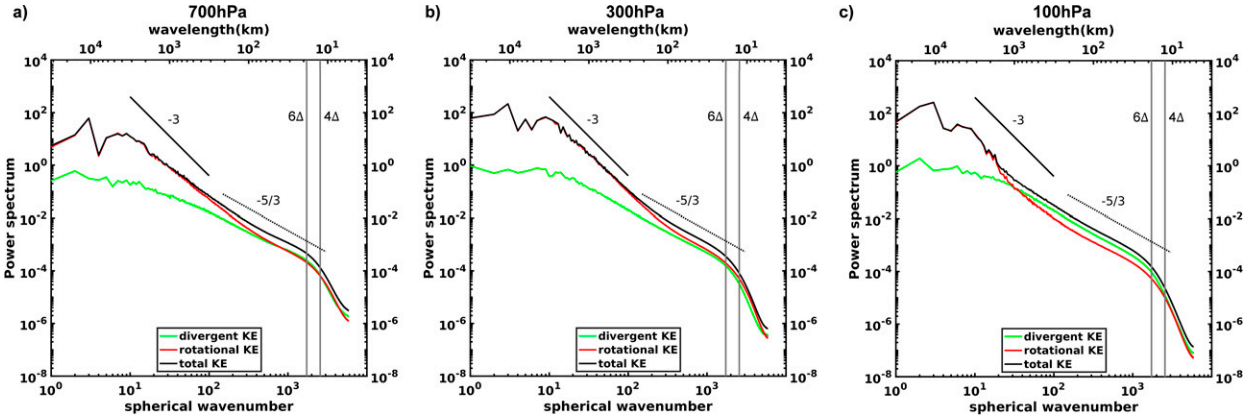

FIG. 1. Kinetic energy power spectra ($m^2\ s^{-2}$) and divergent and rotational components from the 3-km global FV3 control simulation at (a) 700, (b) 300, and (c) 100 hPa.

$$g(s,\mathbf{t},\alpha)=\frac{1}{s^2}\int_{R^2}\psi\left[\mathbf{R}(\alpha)\frac{\mathbf{x}-\mathbf{t}}{s}\right]d\mathbf{x}, \tag{4}$$

where $\mathbf{t}$ is the translation vector and $\mathbf{R}(\alpha)$is the rotation matrix describing a rotation α (Farge 1992). The mother wavelet in Eq. (4) in our study is simple 2D Morlet wavelet (Dallard and Spedding 1993). The simple 2D Morlet wavelet in space domain can be defined as follows:

$$\psi(\mathbf{x})=e^{i\mathbf{k}_0\mathbf{x}}e^{-|\mathbf{x}|^2/2}, \tag{5}$$

(Dallard and Spedding 1993; Antoine et al. 2004), where $|\mathbf{k}_0|$ is the "central wavenumber," and governs the resolution of Morlet wavelets in both space and spectral domains. Smaller values of $|\mathbf{k}_0|$ (generally taken to be $|\mathbf{k}_0|<5$) provide better spatial resolution but worse wavenumber resolution, and vice versa (Addison 2002).

The 2D wavelet power spectra were obtained by first computing the Morlet wavelet coefficients at different azimuth angles, $g(s,\mathbf{t},\alpha)$. The power spectrum at location $\mathbf{x}$ and azimuth angle α is given by

$$P(s,\mathbf{x},\alpha)=|g(s,\mathbf{x},\alpha)|^2. \tag{6}$$

The wavelet power spectrum at location $\mathbf{x}$ can be derived from the superposition of Eq. (6) over azimuth angle:

$$P(s,\mathbf{x})=\frac{1}{N_\alpha}\sum_{j=1}^{N_\alpha}P(s,\mathbf{x},\alpha_j), \tag{7}$$

where $\alpha_j=(N_\alpha-1)\delta\alpha$, $\delta\alpha$ is the angular interval, and N_α is the number of Morlet wavelets in analysis.

In this study, we performed 2D CWT with BT fields to explore the dynamical source of spectral power at different scales. A value of 3.14 for $|\mathbf{k}_0|$ was selected to provide adequate spatial resolution and wavenumber resolution. To better analyze the results in physical space, the scale parameter s was converted to equivalent Fourier based on peak wavenumber method, which gives the wavenumber and wavelength at which the wavelet's spectrum is a maximum (Addison 2002; Kirby 2005). The equivalent Fourier wavelength λ_F of the simple Morlet wavelet analysis at scale s is given by

$$\lambda_F=\frac{2\pi s}{|k_0|} \tag{8}$$

(Kirby 2005). The Morlet wavelet power distribution at the equivalent Fourier wavelength of 30, 252, and 1212 km were selected to represent the spatial distribution of wavelet power at convective scale, mesoscale, and synoptic scale and to analyze the dynamic source of energy at these scales.

4. Results

a. KE spectra and comparison with previous work

Figure 1 exhibits the spectra of the divergent, rotational, and total horizontal KE at 100, 300, and 700 hPa from the 3-km FV3 control simulation. The spectra of the total KE are the sum of the divergent and rotational spectra. The spectra at all three levels exhibit the general characteristics of KE spectra in both modeling (Skamarock 2004; Skamarock et al. 2014; Judt 2018) and observational studies (Nastrom and Gage 1985; Lindborg 1999). At global scales (>2000 km), rotational KE dominates over divergent KE and the spectra of total KE exhibit a shallow slope. The spectra of the total KE clearly illustrate the $\mathbf{k}^{-3}$ segment at the synoptic scale (between ~2000 and ~500 km) and $\mathbf{k}^{-5/3}$ segment at the mesoscale (<500 km), consistent with Skamarock et al. (2014) and Judt (2018). The spectral slope at the scales under 6Δ steepens due to the influence of model filters (Skamarock 2004), and thus the model's effective resolution estimated through KE spectra is 6Δ. The transition between $\mathbf{k}^{-3}$ and $\mathbf{k}^{-5/3}$ segments occurs at longer wavelengths in the stratosphere than in the troposphere, in agreement with Skamarock et al. (2014) and Judt (2018).

The decomposition of KE spectra reveals respective contributions of divergent and rotational component in total KE spectra. In the troposphere, the slope of divergent KE remains shallow close to −5/3 at different levels at the mesoscale. In the lower stratosphere (Fig. 1c), the divergent

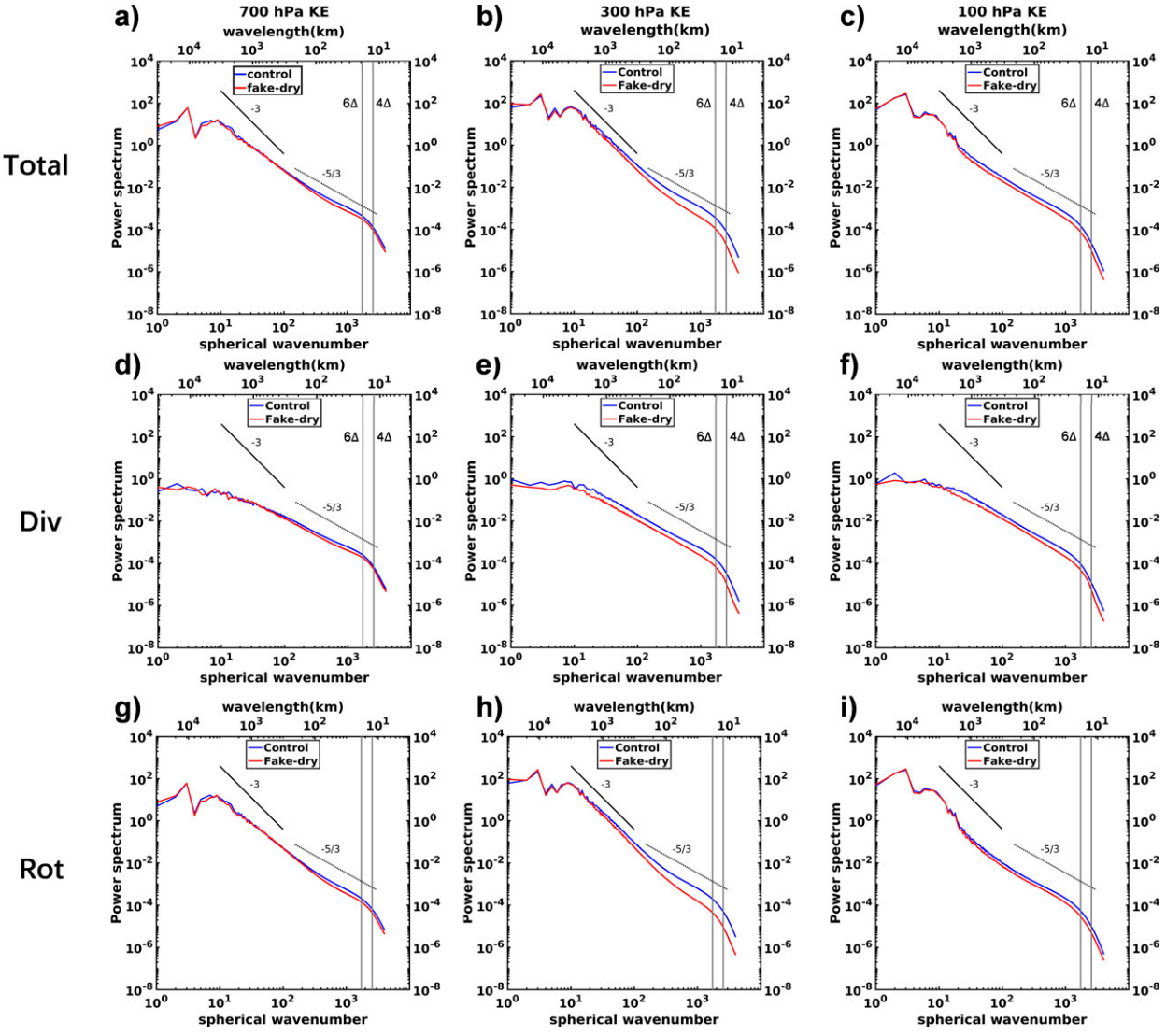

FIG. 2. The comparison of (a)–(c) total kinetic energy power spectra ($m^2 s^{-2}$) and (d)–(f) their divergent and (g)–(i) rotational components between the 3-km control simulation and fake-dry simulation at (left) 700, (center) 300, and (right) 100 hPa.

component with a shallower slope (~−5/3) dominates over the rotational component at the mesoscale and part of the synoptic scales. This behavior is attributed to the vertical transport of energy through gravity waves generated by convection (Sun and Zhang 2016; Waite and Snyder 2009). In the troposphere, rotational components with steeper slopes (~−3) are significantly stronger than divergent components in the synoptic scales, while both rotational and divergent components are nearly equally responsible for the mesoscale −5/3 spectra of total KE. This is in agreement with results using the Model for Prediction Across Scales (MPAS) simulations (Skamarock et al. 2014; Judt 2018) and the idealized simulations of deep moist convection (Sun et al. 2017). The slightly higher amplitude of rotational KE than divergent KE in the troposphere at the mesoscale may be because of the mesoscale convective vortices generated by mesoscale convective systems (MCS) (Davis and Weisman 1994).

A detailed examination of the role of convection in KE spectra is explored through the comparison of KE spectra and their divergent and rotational contributions between the control simulation and 3-km fake-dry simulation presented in Fig. 2. The convection was suppressed in the fake-dry simulation because the effects of latent heating of the condensate in the microphysics were turned off. At 700 hPa, the KE in the fake-dry simulation (Fig. 2a) is slightly smaller compared to the control simulation at the mesoscale, behavior approximately equally attributed to the decrease in divergent (Fig. 2d) and rotational KE (Fig. 2g). At 300 hPa, the KE (Fig. 2b) difference between the fake-dry and the control simulation becomes significantly larger at the mesoscale, while small differences can be found at the synoptic scale. Notably

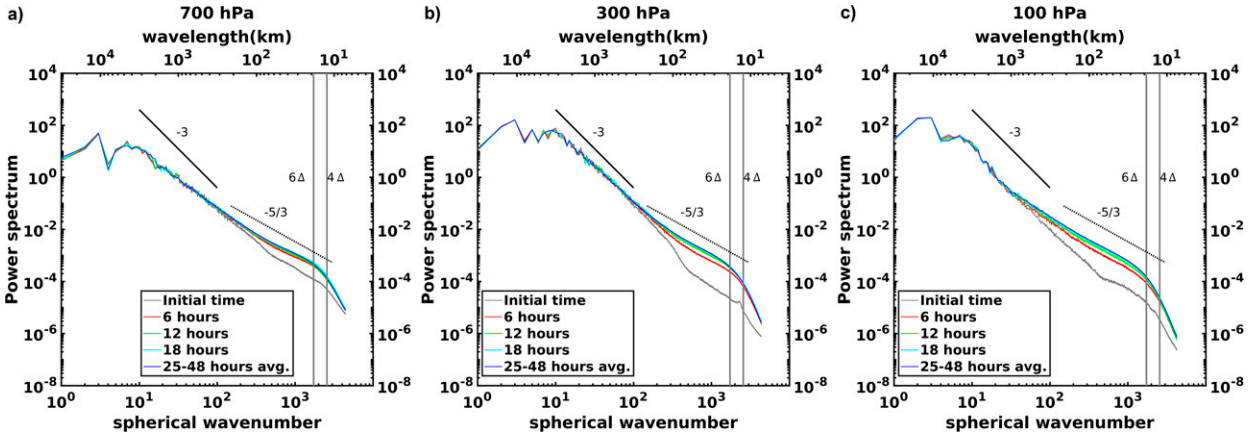

FIG. 3. KE spectra (m^2 s^{-2}) at (a) 700, (b) 300, and (c) 100 hPa for the 3-km FV3 control simulations at simulation times 1 h (gray), 6 h (red), 12 h (green), 18 h (cyan), and 25–48 h average (blue).

the slope of the KE spectrum in the fake-dry simulation becomes steeper at wavenumbers between 300 and 600, compared to the control simulation. The transition scale from −3 to −5/3 increases from wavenumber 300 for the control simulation to about wavenumber 600 in the fake-dry simulation. The decrease of rotational KE (Fig. 2h) is much larger than the decrease of divergent KE (Fig. 2e) at the mesoscale. Under the fake-dry environment, the slope of rotational KE spectrum (Fig. 2h) at the mesoscale increases from about −5/3 to close to −3, while the slope of divergent KE spectrum (Fig. 2e) remains shallow near −5/3 and the amplitude decreases at both the synoptic and mesoscale. At 100 hPa, the KE difference (Fig. 2c) at the mesoscale becomes smaller than that at 300 hPa while still larger than that at 700 hPa, and also expanded into synoptic scale near the wavelength of 1000 km. The slope of the KE spectrum in the fake-dry simulation remains about −5/3 in the mesoscale. The KE differences are predominantly contributed by the differences in divergent KE (Fig. 2f). This behavior is consistent with the results in Hamilton et al. (2008, their Fig. 12 and 13) using the aquaplanet simulation and the dry dynamic core simulation and the results in Sun et al. (2017, their Fig. 11) using moist and dry simulations. Hamilton et al. (2008) also found moist processes and motions by latent heat release contribute to the KE in the mesoscale. The different influence of the convection on KE spectra at different levels is likely explained by the hypothesis that the absence of latent heating feedback first impacts the air temperature in the convective updraft, and hence buoyancy, divergence at the upper troposphere, the strength of the circulation, which ultimately affects the divergence at the lower troposphere. Weaker convection and less energy at the upper troposphere also results in weaker gravity waves entering the lower stratosphere. Thus the impacts of deep moist convection on KE spectrum should be concentrated on the mesoscale in the upper troposphere and the lower stratosphere based on the hypothesis. Sun and Zhang (2016) also found that buoyancy production is the primary mechanism that convection injects energy in the mid- and upper troposphere.

The predictability is closely connected to the KE spectrum. The increase of the spectral slope in the upper troposphere from the control simulation to the fake-dry simulation indicated that deep moist convection plays an important role in mesoscale predictability at the upper troposphere. Buoyancy production in convection at the upper troposphere and its impacts on the divergence at the lower stratosphere and the lower troposphere may contribute to the formation of the mesoscale KE spectrum.

The KE spectra can also be used to examine the spinup time of a NWP model. The evolution of 3-km FV3 KE spectra at three different altitudes are presented in Fig. 3. The results indicate that the spinup time in both the troposphere and stratosphere for FV3 is between 12 and 18 h. This spinup time is similar to that for MPAS between 12 and 18 h in Skamarock et al. (2014) and the theoretical estimate of 16 h in Hamilton et al. (2008).

b. *Regional BT spectra*

Moist convection is often associated with cold brightness temperature at the cloud top. Infrared BTs are very sensitive to absorption and emission of infrared radiation associated with moisture and hydrometeors. There are significant differences in infrared BT between cloudy sky and clear sky. Thus BT and its power spectrum are used in this section to study the role of deep moist convection in the energy spectrum. Infrared BT from *GOES-16* observations, the 3-km control simulation, and fake-dry simulation over the "well-observed" region, and their power spectra are analyzed in this section. The well-observed region refers to the region where satellite sensor zenith angle is less than 60° and cloud features are well observed by *GOES-16* with fine resolution.

BT fields from *GOES-16*, the control simulation, and the fake-dry simulation over the well-observed region are presented in Fig. 4. Cloud features were realistically simulated by the control simulation over the well-observed region (Fig. 4b), in comparison to what was observed by *GOES-16* (Fig. 4a). Specifically, the convection-permitting FV3 successfully simulated tropical convection over the eastern Pacific

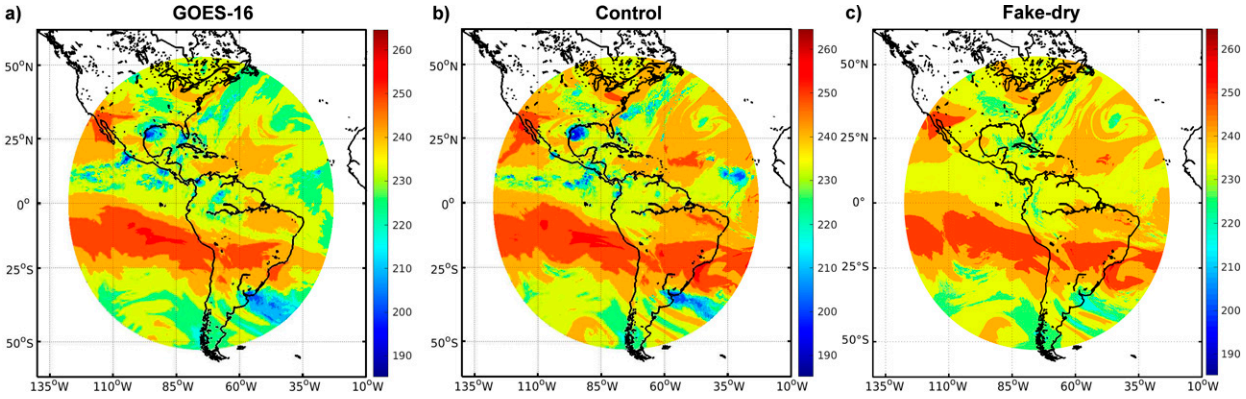

FIG. 4. Brightness temperature from (a) *GOES-16*, (b) 3-km control simulations, and (c) fake-dry simulation in the "well-observed" region (refers to the region with the sensor zenith angle less than 60°) in channel 8 at 1300 UTC 25 Aug 2017.

Ocean and the Amazon basin, Tropical Cyclone Harvey over the Gulf of Mexico, and convection in the South Atlantic Ocean near 50° W. However, there are still some differences. Compared to *GOES-16*, the control simulation has colder BTs in the Tropical Cyclone Harvey. In the North Atlantic Ocean near 30° W, the control simulation has larger patches of cold BT and colder BT minima than the observed. These suggest larger clouds and higher-than-observed cloud top. In the eastern Pacific Ocean, Amazon basin, and South Atlantic Ocean, the simulated clouds have generally lower BTs with higher cloud top and are dislocated compared to the observed. Compared to *GOES-16* and the control simulation, BTs in the fake-dry simulation (Fig. 4c) are generally warmer because deep moist convection is suppressed through turning off diabatic heating. Specifically, only shallow clouds are found in the South Atlantic Ocean, the North Atlantic Ocean, and the Gulf of Mexico, and no brightness temperatures of less than 210 K are seen over the well-observed region.

The histograms of simulated and observed BT (Fig. 5) allow to go a step further to the quantitative comparison. The coldest part of the histogram, below 220 K, for the control simulation agrees well with that for *GOES-16*, indicating the simulated hydrometeors content and intensity of convection appear realistic compared to the observations. The control simulation does not succeed in simulating high brightness temperatures above 230 K, and the difference between the control simulation and the *GOES-16* looks like a simple shift. The difference is likely explained by the failure of the control simulation in generating realistic cloud features in the North Atlantic Ocean. The fake-dry simulation barely generated cold brightness temperature below 220 K, consistent with only shallow clouds found in the Atlantic Ocean and the Gulf of Mexico in Fig. 4. The high brightness temperature part for the fake-dry simulation is generally similar to that for the control simulation.

Figure 6 shows power spectra of BT over the well-observed region for *GOES-16*, the control simulation, and the fake-dry simulation given in Fig. 4. Note that the power spectra were computed over the globe and BTs in the remainder of the globe were zero padded. The BT spectra were plotted as compensated spectra ($\times k^{5/3}$) to more easily identify the subtle differences in both spectral slope and amplitude. The observed *GOES-16* BT spectrum (Fig. 6a) exhibits a shallow slope close to $-5/3$ at wavenumbers between about 50 and 300, followed by a steeper-slope region at wavenumbers greater than 300. The BT spectrum for the control simulation (Fig. 6a) also has a shallow slope near $-5/3$ between wavenumbers about 50 and 300, followed by a transition to another shallow-sloped region with an increase in compensated BT power at wavenumbers from 300 to about 500. The slope steepens at wavenumbers greater than 500 (Fig. 6b). The small peak near wavenumber 500 might result from the accumulation of energy in the cloud top due to the existence of anvil clouds. The small-scale features of new convection on the cloud top are usually obscured by anvil clouds and only affects the mean cloud-top BT. Compared to the control simulation, the BT spectrum for the fake-dry simulation has a much steeper slope near -2 at wavenumbers between 30 and 100 (synoptic).

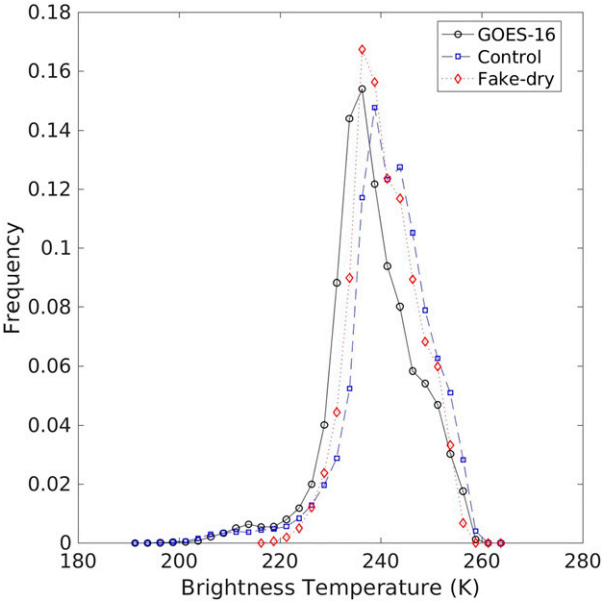

FIG. 5. Histogram of the brightness temperature depicted in Fig. 4.

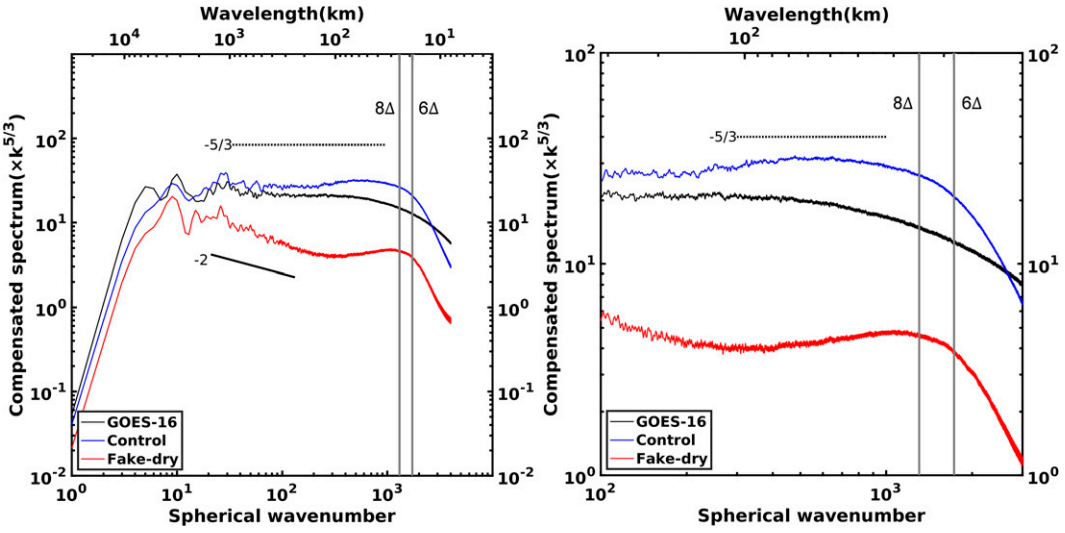

FIG. 6. Unfiltered compensated power spectra ($\times k^{5/3}$; $K^2\ m^{-5/3}$) of BT over the well-observed region for *GOES-16*, the control simulation, and the fake-dry simulation: (left) the full range and (right) zoomed in to emphasize the mesoscale subrange (wavenumber ≥ 100).

The spectral slope for the fake-dry simulation becomes shallower near −5/3 between wavenumbers 200 and 1000. The steeper slope at the synoptic scale might result from the lack of deep convective systems in the fake-dry simulation (Fig. 6c). The small peak near the filter scale is likely associated with grid-scale convection, and other marginally or under-resolved small-scale cloud features.

The spectral slopes for *GOES-16* and the control simulation given in Fig. 6 are further explored in Fig. 7. The spectral slope at wavenumber n was computed by taking differences across $n - 20$ and $n + 20$ (Hamilton et al. 2008). The slope of the *GOES-16* BT spectra is near −5/3 at wavenumbers between 60 and 300, and becomes steeper at wavenumbers greater than 300. The spectral slope for the control simulation generally agrees well with that for *GOES-16* at wavenumbers from 300 to 1300. A small peak is evident near wavenumber 200 in the spectral slope for both *GOES-16* and the control simulation. The spectral slope for the control simulation is slightly steeper than that for *GOES-16* at wavenumbers near 200. This might result from simulated deeper clouds with colder BT over larger patches shown in Fig. 4b compared to *GOES-16*. The steepening of both BT spectra at wavenumbers from 300 to 1300 may be attributed to the smoothing of cloud-top BTs by anvil clouds. Existing anvil clouds can obscure the cooling effect of new convection on cloud-top BTs at convective scales, while becoming slightly cooler and expanding over larger patches due to the upward transport of moisture by new convection. This anvil effect then reduces the energy input from convection into the convective scale, increases the energy input at the scale of anvil clouds near the wavelength of 100 km, and thus increases the slope between wavenumbers 300 and 1300. The spectral slope for the control simulation becomes much steeper than that for *GOES-16* at wavelengths of 6–8Δ (i.e., 18–24 km). The effective resolution is defined as the scale at which the model spectrum starts to decay relative to the observed spectrum (Skamarock 2004). Given the departure of simulated BT spectrum from the observed spectrum in the amplitude within a reasonable range (shown later), the effective resolution can be determined by the departure in the spectral slope. Thus the effective resolution for the FV3 using BT spectra is between 6 and 8Δ.

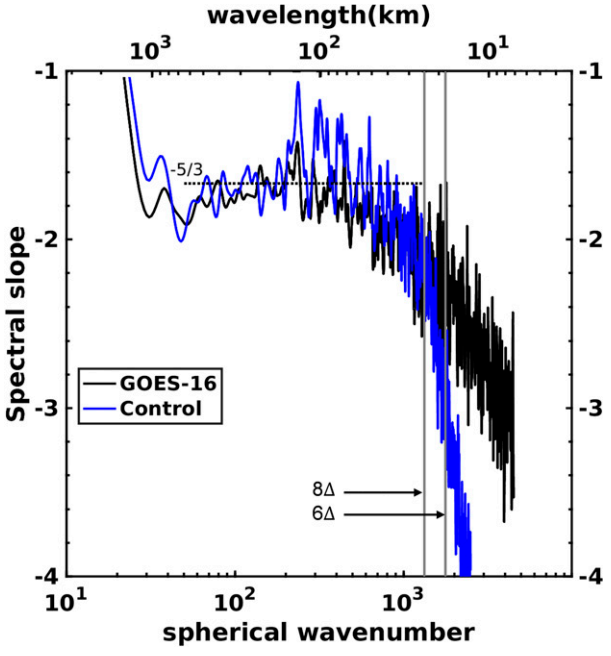

FIG. 7. Slopes for the brightness temperature spectra for *GOES-16* and the control simulation depicted in Fig. 6.

The spectral power of BT for the control simulation (Fig. 6a) is about a factor of 1.3 greater than that for *GOES-16* at wavenumbers between about 50 and 300. The difference increases to

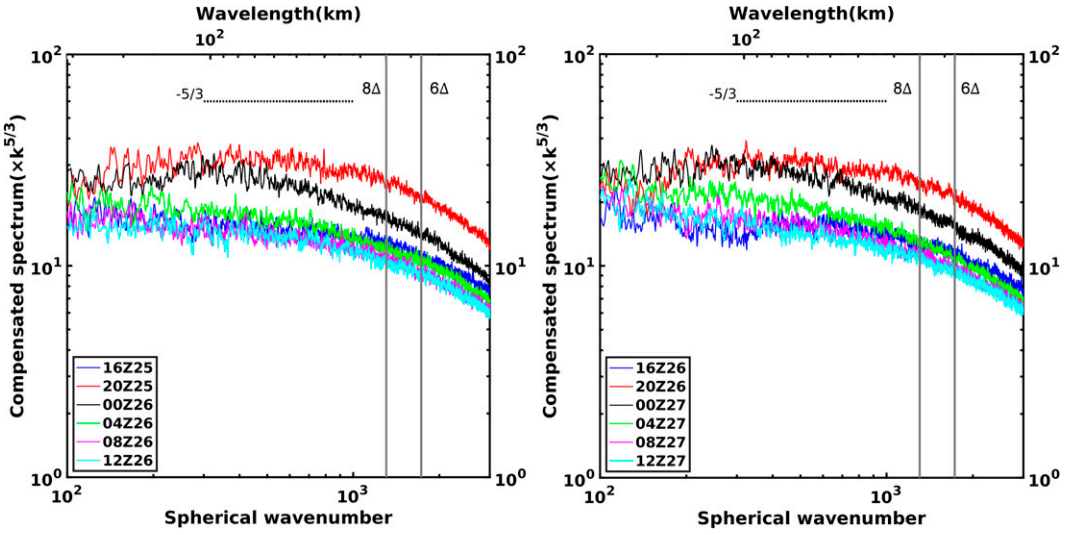

FIG. 8. Unfiltered compensated power spectra ($K^2\ m^{-5/3}$) for *GOES-16* BT at times (left) from 1600 UTC 25 Aug to 1200 UTC 26 Aug 2017 and (right) 1600 UTC 26 Aug to 1200 UTC 27 Aug 2017 every 4 h.

about 1.6 at wavenumbers near 500 (Fig. 6b), and starts to decrease at 6–8Δ. The differences in the spectral power of BT between *GOES-16* and the control simulation can be explained by their differences in BT fields. Specifically, the simulated colder BT in Tropical Cyclone Harvey and moist convection over the North Atlantic Ocean should be responsible for the larger spectral power for the control simulation compared to the observed. The dislocation and higher intensity of clouds in eastern Pacific Ocean and Amazon basin might also be responsible for the differences in both spectral power and spectral slope. The increase of the difference between wavenumber 300 and wavenumber 500 can also be partially explained by the effect of anvil clouds. The accumulation of moisture transported by deep moist convection in anvil clouds can expand the coverage of anvil clouds and slightly cools cloud-top BTs, resulting in more energy input at wavenumbers between 300 and 500. The spectral power of BT for the control simulation (Fig. 6a) is about a factor of 3 greater than that for the fake-dry simulation at the wavenumber 30. The difference increases to about 7 at wavenumbers about 300 and starts to decrease at the wavenumber near 1000. The lack of deep moist convection in the BT field in the fake-dry simulation (Fig. 4c) compared to the control simulation (Fig. 4c) implies that deep moist convection plays an important role in energizing the BT spectrum in both mesoscale and synoptic scale. More details will be discussed in section 4c.

Chan et al. (2020) also presents the comparison between observed and simulated power spectrum of infrared BT, but using *Meteosat-7* satellite observations and 9-km regional simulations (see their Fig. 5). The observed power spectra and the mean power spectra for the ensemble simulations without data assimilation (NoDA) in their Fig. 5 exhibit a shallow slope near −5/3 at wavelengths between 500 and 200 km, which is in agreement with our results. The simulated BT spectra also show the slight decrease in the spectral slope near the wavelength of 100 km. There are also differences in spectral power between the observed and the simulated spectra at the wavelengths between 500 and 200 km, resulting from the differences in the intensity and location of cloud patterns. These differences are then largely reduced by assimilating the satellite observations. Thus the deviation of the BT spectrum for the control simulation from the observed spectrum in Fig. 6 is reasonable given the fact that data assimilation is not used in our study.

To further explore the variability of the observed BT spectra, Fig. 8 presents the variation of unfiltered observed BT spectra during the simulation period. The spectral power of the observed BT spectra shows large diurnal variations. The peak spectral power of BT at wavenumbers between 200 and 1300 occurs at 2000 UTC 25 August 2017, near the local afternoon. This is consistent with the peak intensity of deep convection in the late afternoon in the summertime at North America found by Tian et al. (2005). The diurnal variation of BT spectra can be attributed to the variations in the intensity and location of cloud patterns of Tropical Cyclone Harvey and convection over the Amazon basin, eastern Pacific Ocean, and South Atlantic Ocean (not shown). The observed BT spectrum at 2000 UTC 25 August 2017 is qualitatively similar to the BT spectrum for the control simulation. Specifically, the compensated spectral power of the observed spectrum also increases between wavenumbers 150 and 300, and then decreases at wavenumbers above 500. The ratio of the spectral power at different times to that of mean observed spectra at wavenumbers between 100 and 1300 ranges from 0.5 to 2. The ratio of the spectral power for the control simulation to that for the observations at the same wavenumbers is from 1.3 to 1.5, within the spread of the ratio for the observed BT spectra and mean observed spectra. Thus the deviation of the BT spectrum for the control simulation from the observed spectra in the amplitude is within a reasonable range given the diurnal variation of observed spectrum.

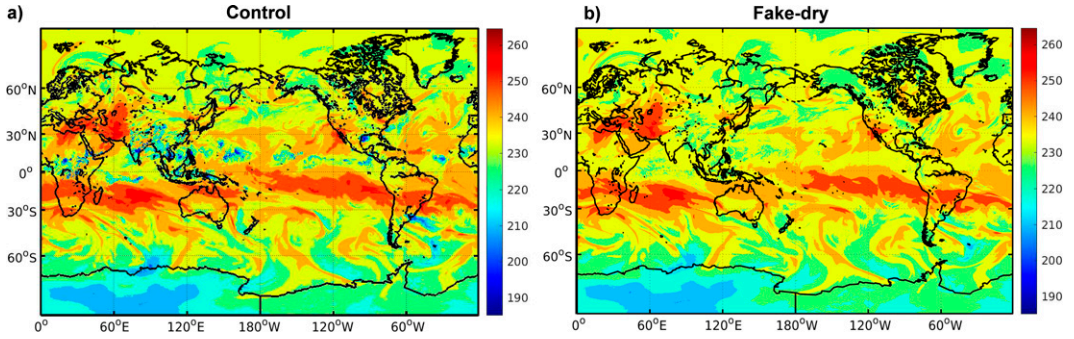

FIG. 9. Global brightness temperature from (a) 3-km control simulations and (b) fake-dry simulation in channel 8 at 1300 UTC 25 Aug 2017.

c. *Global BT spectra*

To further explore the role of moist processes in BT spectra at different scales, global BT fields and BT spectra for the control simulation and the fake-dry simulation are analyzed in this section. 2D CWT is employed to study the connection between the structure of 1D spherical harmonic spectrum of BT and moist processes at convective scale, mesoscale, and synoptic scale, respectively.

The global BTs from the 3-km control simulation and the fake-dry simulation are presented in Fig. 9. The control simulation with moist physics captures major moist processes in the tropics and midlatitudes. In the tropics, deep convection is concentrated in the tropical cyclone in the Gulf of Mexico and convective systems in the intertropical convergence zone (ITCZ), including the tropical Pacific Ocean, the Maritime Continent, the Amazon basin, the Indian Ocean, the North Atlantic Ocean, and Central Africa. In the southern midlatitudes, baroclinic waves are coupled with deep moist convection. In the fake-dry simulation, moist processes are suppressed due to the turnoff of latent heating-cooling effects in the microphysics. Most deep convection in the control simulation was replaced by shallow convection in the fake-dry simulation, including the western Pacific Ocean, the Indian Ocean, the Gulf of Mexico, Amazon basin, and central Africa. In the fake-dry simulation, shallow convection is also found in the North Pacific storm-track region, the midlatitude cyclone in the North Atlantic Ocean and North America, and baroclinic waves in the southern midlatitudes.

To explore the impacts of moist processes on the energy input and spectral slope of BT spectrum, the global power spectra for the BT fields depicted in Fig. 9 are presented in Fig. 10. The global BT spectra show generally similar structures to the BT spectra in Fig. 6 except amplitude. The differences in the amplitude between the global BT spectra and the BT spectra over the well-observed region for both the control and the fake-dry simulation can be largely attributed to the zero-padding of regions except the well-observed region. The global BT spectra for the control simulation show a generally shallow slope near −5/3 between wavenumbers 30 and 1300. The spectral slope becomes much steeper near 6–8Δ. This behavior is basically consistent with the BT spectra over the well-observed region for the control simulation in Fig. 6. The compensated spectral power of global BT slightly decreases at wavenumbers from 30 to about 150 (synoptic scale) with small variations in the spectral slope, which is not evident in the spectrum for the control simulation over the well-observed region in Fig. 6. This behavior might be related to the equatorial waves in the tropics and baroclinic waves in the southern midlatitudes which are not considered in the BT spectra in Fig. 6. The compensated spectral power of global BT slightly increases at the wavenumbers from 200 to 400. The BT spectrum over the well-observed region in Fig. 6 also has similar structure in the wavenumber range, resulting from stronger convection with cooler BT and dislocation of clouds compared to the observed. Since global satellite observations are not available now, it is impossible to estimate the deviation of simulated global BT spectra from the observed global BT spectra directly. We hypothesize that the slight increase of compensated spectral power from wavenumber 200 to

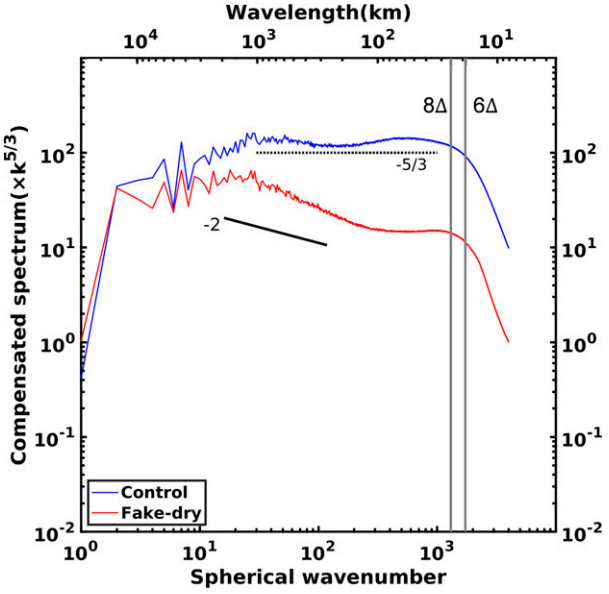

FIG. 10. Compensated global power spectra ($K^2\ m^{-5/3}$) for the BT fields depicted in Fig. 9.

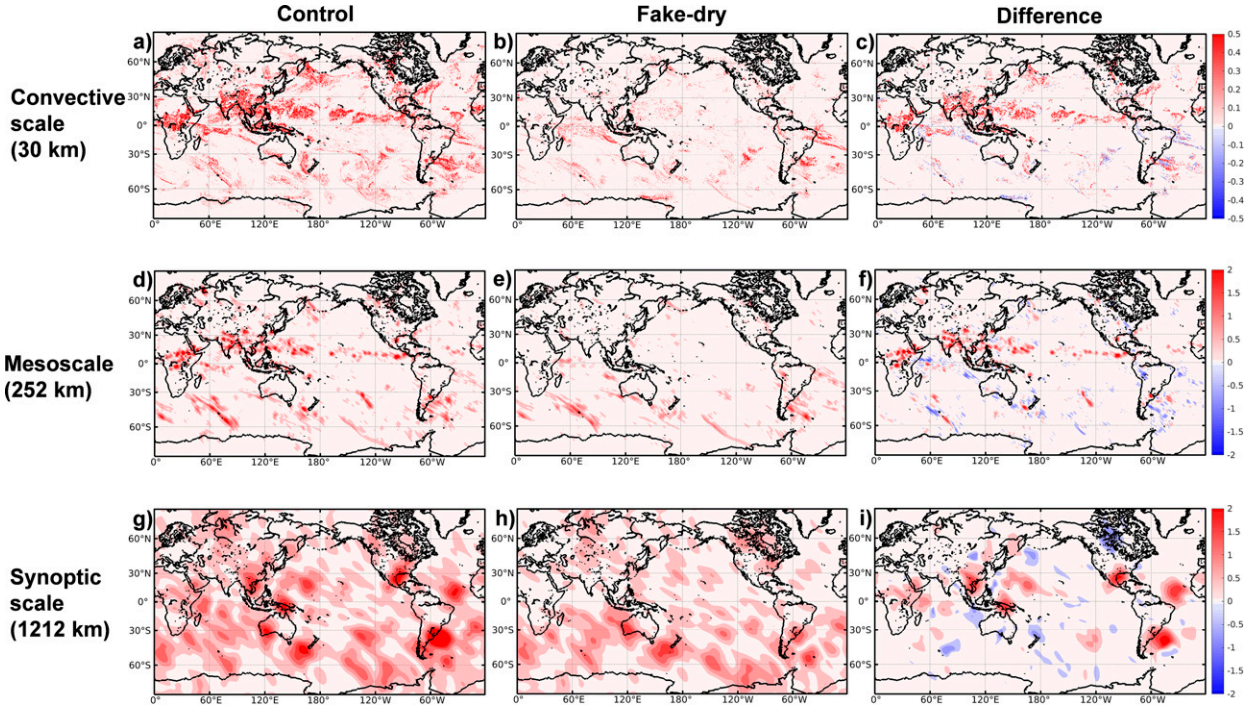

FIG. 11. 2D distribution of wavelet power spectra (K^2) of BT in (a),(d),(g) the 3-km control simulation; (b),(e),(h) fake-dry simulation; and (c),(f),(i) difference (control–fake-dry) between them at the (top) convective scale (30 km), (middle) mesoscale (252 km), and (bottom) synoptic scale (1212 km).

wavenumber 400 in the global BT spectra for the control simulation is also related to the intensity of convection and the location of clouds. Anvil clouds might also play a role in transferring the power of BT at finer scales into the scale at the wavenumber 400. The global BT spectrum for the fake-dry simulation has a more stable spectral slope near −5/3 between wavenumbers 300 and 1300 compared to the control simulation. This also suggests that deep convection and cloud patterns might be responsible for the small variation in the spectral slope and energy transfer within the wavenumber range for the control simulation. The spectral power of global BT for the control simulation is about a factor of 3 greater than that for the fake-dry simulation near the wavenumber 30. The difference increases to 8 near the wavenumber 300. This suggest that moist processes energize the mesoscale and synoptic scale in the BT spectrum. The spectral slope for the fake-dry simulation is much steeper than that for the control simulation between wavenumbers 30 and 300. Thus moist processes like baroclinic waves and tropical equatorial waves are critical in the creation of the shallow BT spectrum at the synoptic scale and part of the mesoscale between wavenumbers 30 and 300.

A detailed examination of the contributions from moist processes at different scales are explored by wavelet analysis. 2D CWT was employed to examine the spatial distribution of the spectral power of BT across spatial scales. Figure 11 exhibits the 2D Morlet wavelet power distribution of BT in the 3-km control simulation, fake-dry simulation, and difference between them at the convective scale, mesoscale, and synoptic scale. The Morlet wavelet power distribution at the equivalent Fourier wavelength of 30, 252, and 1212 km were selected to represent the power distribution at the convective scale, mesoscale, and synoptic scale, respectively.

At the convective scale, the spectral power of BT using wavelet transform for the control simulation (Fig. 11a) is generally consistent with the distribution of convection shown in the BT field (Fig. 9a). Specifically, the spectral power is mainly contributed from convective-scale convection found at the ITCZ, the southern midlatitudes associated with baroclinic waves, the North Pacific storm tracks, and the South and the North Atlantic Ocean. For the fake-dry simulation (Fig. 11b), the spectral power becomes significantly weaker over the globe due to the suppression of deep convection, especially in the ITCZ, the North Pacific Ocean, and the North Atlantic Ocean. The spectral power of BT is concentrated in the Indian Ocean, the southern midlatitudes associated with baroclinic waves, and the South Atlantic Ocean. The differences (Fig. 11c) in the spectral power between the control and the fake-dry simulation are mainly located at regions with convection in the Northern Hemisphere. The differences in the southern midlatitudes are relatively small compared to the differences in the Northern Hemisphere. This suggests that convection associated with baroclinic waves in the southern midlatitudes is not the major source of the differences in the spherical harmonic power spectrum of BT at the convective scale between the control and the fake-dry simulation in Fig. 10. Instead, deep convection in the ITCZ and shallow convection in the North Pacific storm-track region play an

important role in energizing the convective scale in the spherical harmonic power spectrum of BT, and are responsible for the power difference between the control simulation and the fake-dry simulation at the convective scale in Fig. 10. Note some small negative differences can be found in the southern Atlantic Ocean, the Indian Ocean, and the southern midlatitudes associated with baroclinic waves. These differences are likely because in the fake-dry simulation, moisture was transported from the regions that can generate deep convection in the control simulation to other regions to form shallow convection there.

Idealized simulation of moist convection alone in Sun and Zhang (2016) can generate −5/3 KE spectrum through buoyancy production in both mesoscale and convective scale. In the fake-dry simulation, the feedback of latent heating–cooling in the microphysics was turned off, and thus moist convection cannot produce buoyancy through the release of latent heat and develop into deep moist convection. However, the BT spectrum for the fake-dry simulation still shows −5/3 slope at the wavelengths less than 100 km, indicating that deep moist convection is not the critical factor for the creation of the −5/3 slope in the BT spectrum at convective scale. It implies that the role of other dynamics in creating −5/3 KE spectrum at the convective scale is still worth investigation, though the connection between KE and BT spectra is still unclear.

In the mesoscale, the spectral power of BT for the control simulation (Fig. 11d) is mainly associated with mesoscale convective systems (MCSs) in the ITCZ, including the tropical Pacific Ocean, Central Africa, and Maritime Continent, and the southern midlatitudes associated with baroclinic waves. For the fake-dry simulation (Fig. 11e), the spectral power is mainly connected with weak MCSs in the Indian Ocean and the southern midlatitudes associated with baroclinic waves. The differences (Fig. 11f) between the control and the fake-dry simulation are mainly located at tropical Pacific Ocean, Maritime Continent, and central Africa in the tropics and the southern midlatitudes associated with baroclinic waves. Some negative differences in Fig. 11f associated with baroclinic waves in the southern midlatitudes might be related to the transport of moisture from the tropics to the southern midlatitudes through Hadley cells. The positive differences are concentrated in the tropics. Thus MCSs in the tropics are mainly responsible for injecting energy in the mesoscale of spherical harmonic power spectrum of BT for the control simulation in Fig. 10. Durran and Weyn (2016) found that the simulation of convective cloud systems alone can generate mesoscale −5/3 KE spectrum comparable to the observations. Thus mesoscale convective systems are important for providing energy input in the mesoscale for both KE and BT spectra. Waite and Snyder (2013) studied idealized simulations of baroclinic waves and found that moist processes associated with baroclinic waves only impacts the divergent KE but does not influence the spectral slope in the mesoscale in the upper troposphere. Moist processes associated with baroclinic waves also have relatively small impacts on the spectral slope of BT spectra in the mesoscale, which implies that there might be some connections between BT and KE in the upper troposphere.

At the synoptic scale, the spectral power of BT (Fig. 11g) expands into synoptic-scale patches. The spectral power is closely related to equatorial waves in the tropics and baroclinic waves in the southern midlatitudes. For the fake-dry simulation (Fig. 11h), the spectral power is mainly associated with baroclinic waves in the southern midlatitudes. The positive differences (Fig. 11i) between the control simulation and the fake-dry simulation are mainly associated with equatorial waves in the tropics and baroclinic waves in the southern midlatitudes near 60°W. Negative differences are concentrated in the midlatitude cyclone in North America and baroclinic waves in the southern midlatitudes near 90°E and 180°. The negative differences might be generated by the transport of moisture by Hadley cells from the tropics to the midlatitudes, and the adjustment of Rossby waves in the fake-dry simulation due to the lack of the feedback from latent heating. Thus tropical equatorial waves and baroclinic waves in the southern midlatitudes are critical in producing a shallow slope near −5/3 and providing energy in the spherical harmonic power spectrum of BT at the synoptic scale for the control simulation in Fig. 10. The spectral slope near −5/3 for spherical harmonic power spectrum of BT in the synoptic scale is much shallower than the −3 slope of KE spectra.

Convective systems important for the BT spectrum at different scales are closely connected in space. Specifically, deep convection at convective scale, MCSs in the tropical Pacific Ocean and Central Africa in the mesoscale, as well as equatorial waves at the synoptic scale, are all concentrated in similar locations in the tropics. Thus the energy transfer in the BT spectrum between different scales are likely determined by the interaction among convective systems at different scales. Judt (2018) found that initial error growth was closely related to moist convection, and then error grew up in magnitude at all scales. The growth of error at all scales might be related to the interaction among convective systems at different scales. Given the dependence of BT spectra on convective systems, BT spectra can also be used to evaluate the predictability of convective systems at different scales in future studies.

d. Convective parameterization and model physics

Convective parameterization is an important aspect of model configurations that affect the energy spectrum and the simulation of convective upscale effects in coarse-resolution models. Grid spacing on the order of 100 m is required to explicitly resolve convective cells (Bryan et al. 2003). However, modeling studies in X. Chen et al. (2018a,b) indicated that without the parameterization of deep convection, the statistical characteristics of tropical MCSs can still be realistically simulated using a "gray zone" grid spacing (~10 km). When the grid spacing is greater than 10 km, the omission of convective parameterization in the simulation might be problematic, resulting in excessive vertical moisture transport and a slower evolution of convective systems due to the delayed strengthening of the cold pool (Weisman et al. 1997). However, there are also some benefits when not using a convective

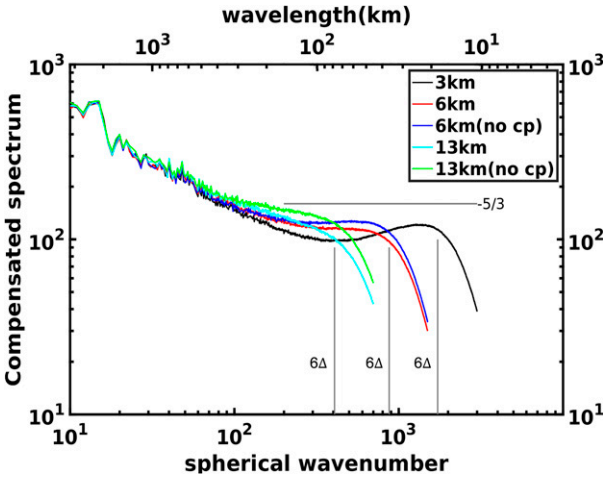

FIG. 12. Compensated power spectra of 700-hPa kinetic energy ($m^{1/3}$ s^{-2}) with and without the parameterization of deep convection (cp).

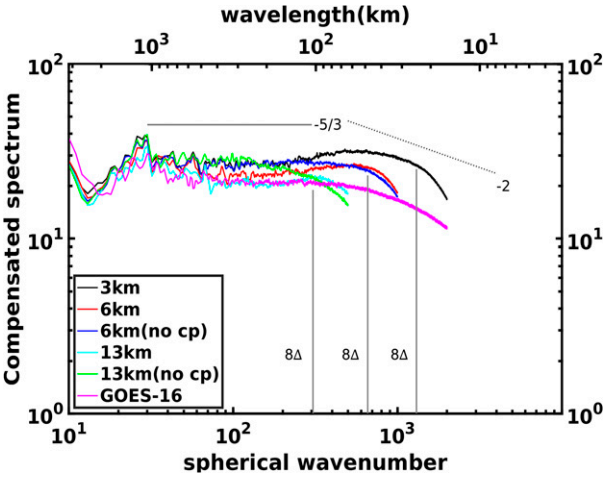

FIG. 13. Compensated power spectra (K^2 $m^{-5/3}$) of brightness temperature over the well-observed region with and without the parameterization of deep convection (cp). *GOES-16* BT spectrum is also included for comparison.

parameterization, such as the propagation of convective systems, and a more realistic circulation pattern due to the stronger convective updraft in the convection area (Weisman et al. 1997).

To further explore the impact of the convective parameterization on the simulated atmospheric power spectra, we performed simulations using 6- and 13-km meshes with and without SAS deep convection parameterization. The compensated tropospheric KE spectra for these simulations are presented in Fig. 12 along with the 3-km spectra for comparison. Between spherical wavenumbers 100 and 400, the KE is about a factor of 2 larger in the 6- and 13-km simulations without deep convection parameterization compared to the 3-km simulation. The magnitude difference is smaller than 2 in the 6- and 13-km simulations with deep convection parameterization. These results are in agreement with the results from the MPAS model (Skamarock et al. 2014, their Fig. 9) and NICAM model (Terasaki et al. 2009, their Fig. 2). Thus, convective parameterization can improve the simulation of KE spectra for the coarse-grid (7.5- and 15-km mesh) simulations in the well-resolved scales of the KE spectrum—that is wavelengths above 6Δ for FV3. For the coarse-grid simulations, the turning off of the deep convection parameterization leads to stronger convective updrafts and convection (not shown), generates more gravity waves in the upper troposphere, and thus increases the mesoscale KE. Malardel and Wedi (2016) also found that the impacts of switching off the deep convection parameterization scheme on mesoscale KE spectrum for a 5-km global simulation is through the available potential energy cascade between wavenumbers 20 and 900 resulted from the wave response to the explicitly simulated convection.

The BT power spectra for these simulations are presented in Fig. 13 based on the BT over the well-observed region to directly compare with the observed. The BT spectra for the 3-km control simulation and *GOES-16* are also included for comparison. The BT spectrum for the 13-km simulation with deep convection parameterization scheme agrees well with *GOES-16* BT spectrum in both magnitude and spectral slope at wavelengths above 8Δ. The BT spectrum for the 13-km non-parameterized convection simulation is about a factor of 1.2 greater than *GOES-16* BT spectrum between wavenumbers 80 and 300. This is attributed to the stronger MCS simulated in the non-parameterized convection simulation (not shown). The BT spectra for the 6-km parameterized convection simulation and *GOES-16* BT spectrum start to diverge near wavenumber 100 and their difference increases to about a factor of 1.3 near 8Δ. The BT spectrum for the 6-km non-parameterized convection simulation is about a factor of 1.3 greater between wavenumbers 100 and 600 compared to *GOES-16* BT spectrum. The deep convection parameterization scheme seems to constrain the development of mesoscale convective systems at the scales above 100 km. The similar behavior for both spectra between wavenumber 300 and 600 suggests that no matter whether the deep convection parameterization scheme is turned off or not for the 6-km simulations, FV3 seems to overestimate the intensity of convection at the wavelengths less than 100 km. Interestingly, the 6-km non-parameterized convection simulation generated a similar shallow spectral slope near −5/3 between wavenumber 100 and 600 as found in *GOES-16* BT spectrum, while the BT spectrum produced by the 6-km parameterized convection simulation has a closer spectral power but a shallower slope compared to *GOES-16* BT spectrum in the same range. This suggests that turning off the deep convection parameterization scheme for the 6-km simulation can better capture the dynamics in the mesoscale, while the use of deep convection parameterization can partially improve the simulation of the intensity of convection.

Malardel and Wedi (2016) suggested that when the deep convection parameterization scheme is turned off, the coupling between the dynamics and the cloud microphysics scheme is responsible for the release of convective available potential energy. Thus the coupling of the cloud microphysics

scheme and the dynamics is responsible for the overestimate of the intensity of convection in the mesoscale and convective scale. Chan et al. (2020) found that data assimilation of infrared BT can improve the simulation of the intensity and location of clouds, and thus largely reduce the differences in the mesoscale of the BT spectra between a 9-km regional simulation without deep convection parameterization and satellite observed BT spectrum. Thus data assimilation of BT can potentially improve the simulation of convective systems and cloud patterns in the coarse-grid simulations.

5. Summary

This study investigates the role of convection in atmospheric kinetic energy spectra and brightness temperature spectra by connecting global convection-permitting FV3 model simulations with high-resolution *GOES-16* satellite observations. The main goals of this study are to 1) investigate the role of deep moist convection in mesoscale −5/3 KE spectra, 2) explore the role of deep moist convection in BT spectra, and 3) examine the dependence of the BT spectrum on convective systems across scales. Specifically, the role of convection is explored through examining the differences in the BT and KE spectra between the 3-km control simulation and fake-dry simulation for the 3-day period from 24 to 27 August 2017. The fake-dry simulation was performed with latent heating-cooling feedback switched off in the microphysics scheme to suppress the formation of deep convection. 2D wavelet power spectra of BT for the control simulation and the fake-dry simulation are used to explore how convective systems at different scales impact BT spectra. Findings from this study are summarized as follows:

1) FV3 KE spectra show a steep slope near −3 at the synoptic scale and a shallow slope near −5/3 in the mesoscale. This behavior is qualitatively similar to the KE spectra from other observational and modeling studies.
2) The influence of deep moist convection on mesoscale KE spectrum is concentrated on the upper troposphere and the lower stratosphere. The impacts of deep moist convection on the lower troposphere is relatively small. This can be explained by the influence of latent heating in the microphysics on the simulation. In the fake-dry simulation, the absence of latent heating effects first impacts the air temperature in the convective updraft, and hence buoyancy production, divergence at the upper troposphere, the strength of the circulation, which ultimately affects the divergence at the lower troposphere. Weaker convection and buoyancy production at the upper troposphere also results in weaker gravity waves entering the lower stratosphere. Thus the absence of latent heating feedback has more direct impacts on the upper troposphere and the lower stratosphere than the lower troposphere. Deep moist convection can energize the mesoscale and change the shallow slope in the mesoscale of KE spectra at the upper troposphere, which implies that convection is important in the limit of mesoscale predictability.
3) The spectrum of BT over the well-observed region for the control simulation has a similar shallow slope near −5/3 in the mesoscale as that for *GOES-16* BT spectrum. The spectral slope for both spectra slightly increases from −5/3 at the wavelength near 100 km to −2 near 8Δ (i.e., 24 km). The increase in the slope might be attributed to the effect of anvil clouds. Anvil clouds can obscure the cooling effect of new convection on cloud-top BTs at convective scales, and thus reduce the energy input due to deep moist convection at the convective scale. The spectral power of BT for the control simulation is greater than that for *GOES-16*, due to the dislocation and higher intensity of simulated convection compared to the observed.
4) *GOES-16* BT spectra exhibit a relatively large diurnal variability. This variability is attributed to the diurnal variation of the intensity of convection. The spectral power of BT is largest near the local afternoon, consistent with the peak intensity of deep convection in the late afternoon in the summertime at North America found by Tian et al. (2005).
5) The effective resolution for FV3 estimated using the BT spectrum is 6–8Δ. The differences in the spectral power between *GOES-16* and the control simulation are relatively stable across scales and within the range of diurnal variation of observed BT spectrum. Thus the effective resolution is determined by the departure of the spectral slope for the control simulation from that for *GOES-16*. The filter scale of 6–8Δ is also evident in the BT spectra for the coarse-grid (6- and 13-km) simulations (Fig. 13).
6) Moist processes energize the mesoscale and the synoptic scale for global BT spectrum. The spectral power of global BT for the control simulation is significantly greater in the mesoscale and the synoptic scale than that for the fake-dry simulation. The spectral slope of BT for the fake-dry simulation is much steeper than that for the control simulation. Thus synoptic-scale moist processes like baroclinic wave and tropical equatorial wave are critical in the creation of the shallow BT spectrum at the synoptic scale.
7) BT spectrum is dependent on convective systems at different scales. Deep convection in the ITCZ and shallow convection in the North Pacific storm-track region play an important role in energizing the convective scale of the BT spectrum. In the mesoscale, the BT spectrum for the control simulation is mainly energized by mesoscale convective systems (MCSs) in the ITCZ. Tropical equatorial waves and baroclinic waves in the southern midlatitudes are critical in producing the shallow slope near −5/3 and providing energy in the BT spectrum at the synoptic scale.
8) The simulation of the intensity of convective systems is still an issue for numerical weather prediction models at a grid spacing less than 6 km when deep convection parameterization scheme is not used. The 3-km control simulation and the 6-km simulations without deep convection parameterization both generated larger spectral power at the wavelengths lower than 100 km compared to *GOES-16*, resulted from overestimated intensity of convection at convective scale. The use of a deep convection parameterization

scheme in the 6-km simulation can constrain the spectral power of BT at the wavelengths above 100 km, but result in a much shallower slope than the observed, indicating the bias in the structure of simulated convective systems.

These findings encourage the future development in cloud microphysics and deep convection parameterization, and data assimilation to improve the intensity and the structure of simulated convective systems. However, there are some caveats in our study. The vertical resolution employed in this study is relatively coarse. Skamarock et al. (2019) indicated that a vertical mesh spacing of 200 m is required to attain solution convergence, and the mesoscale KE increases as vertical resolution is increased until convergence. Thus the underresolution in the vertical in this study might decrease the mesoscale KE and impact the robustness and the generality of the results. The influence of vertical resolution on BT spectra is worth investigation.

The connection between KE and BT spectra is not fully understood. The shallow slope near −5/3 for BT spectra is qualitatively similar to that for divergent KE spectra in the upper troposphere and lower stratosphere. Thus we hypothesize that BT spectra might have some connections with divergent KE spectra in the upper troposphere and the lower stratosphere. BT spectra are dependent on convective systems at different scales, while convection and convection-generated gravity waves are important sources of mesoscale KE in the lower stratosphere (Sun and Zhang 2016). However, the impacts of deep convection on BT spectra are much greater than those for divergent KE spectra at the stratosphere and the troposphere based on the comparison between the control simulation and the fake-dry simulation. More work is needed.

The uncertainties in CRTM due to the constant sensor zenith angle, hydrometer scattering properties, and other parameters may have impacts on the simulated BTs, especially the BT for convective systems. The development of CRTM in future studies might also improve the simulated BT for deep moist convection and convective systems.

Given the dependence of BT spectra on convective systems, BT spectra can potentially be used to explore the predictability of convective systems at different scales. The explanation of the shallow slope and the role of shallow convection in the BT spectra is also worth future investigation. The ability of models to generate BT spectra comparable to that produced by satellite observations could be an important aspect for the development of model dynamics and cloud microphysics scheme.

Acknowledgments. The authors benefited from insightful conversations with Yunji Zhang and Yongqiang Sun, and especially their assistance in generating initial conditions for FV3 simulations. Funding was provided by the National Science Foundation Grant AGS-1712290 and NOAA Next Generation Global Prediction System grant through University of Michigan Subcontract 3004628721. Most of the computing for this project was performed on the Stampede2 supercomputer at the Texas Advanced Computing Center.

Data availability statement. All data in this study are publicly available. *GOES-16* data are available at https://www.avl.class.noaa.gov/saa/products/search?sub_id=0&datatype_family=GRABIPRD&submit.x=22&submit.y=6. Output from the FV3 simulations are publicly archived at https://doi.org/10.26208/aesc-9y07

REFERENCES

Addison, P. S., 2002: *The Illustrated Wavelet Transform Handbook*. 1st ed. CRC Press, 368 pp.

Antoine, J.-P., R. Murenzi, P. Vandergheynst, and S. T. Ali, 2004: *Two-Dimensional Wavelets and Their Relatives*. Cambridge University Press, https://doi.org/10.1017/CBO9780511543395.

Arakawa, A., and W. H. Schubert, 1974: Interaction of a cumulus cloud ensemble with the large-scale environment, part I. *J. Atmos. Sci.*, **31**, 674–701, https://doi.org/10.1175/1520-0469(1974)031<0674:IOACCE>2.0.CO;2.

Bryan, G. H., J. C. Wyngaard, and J. M. Fritsch, 2003: Resolution requirements for the simulation of deep moist convection. *Mon. Wea. Rev.*, **131**, 2394–2416, https://doi.org/10.1175/1520-0493(2003)131<2394:RRFTSO>2.0.CO;2.

Cavanaugh, N. R., T. A. O'Brien, W. D. Collins, and W. C. Skamarock, 2017: Spherical harmonic spectral estimation on arbitrary grids. *Mon. Wea. Rev.*, **145**, 3355–3363, https://doi.org/10.1175/MWR-D-16-0259.1.

Chan, M.-Y., F. Zhang, X. Chen, and L. R. Leung, 2020: Potential impacts of assimilating all-sky satellite infrared radiances on convection-permitting analysis and prediction of tropical convection. *Mon. Wea. Rev.*, **148**, 3203–3224, https://doi.org/10.1175/MWR-D-19-0343.1.

Chen, J.-H., and S.-J. Lin, 2013: Seasonal predictions of tropical cyclones using a 25-km-resolution general circulation model. *J. Climate*, **26**, 380–398, https://doi.org/10.1175/JCLI-D-12-00061.1.

——, X. Chen, S.-J. Lin, L. Magnusson, M. Bender, L. Zhou, and S. Rees, 2018: Tropical cyclones in GFDL fvGFS—Impacts of dycore, physics and initial conditions. *33rd Conf. on Hurricanes and Tropical Meteorology*, Ponte Vedra, FL, Amer. Meteor. Soc., 9B.4, https://ams.confex.com/ams/33HURRICANE/webprogram/Manuscript/Paper339827/9B.4_extended_abstract.pdf.

——, S.-J. Lin, L. Zhou, X. Chen, S. Rees, M. Bender, and M. Morin, 2019: Evaluation of tropical cyclone forecasts in the next generation global prediction system. *Mon. Wea. Rev.*, **147**, 3409–3428, https://doi.org/10.1175/MWR-D-18-0227.1.

Chen, X., O. M. Pauluis, and F. Zhang, 2018a: Regional simulation of Indian summer monsoon intraseasonal oscillations at gray-zone resolution. *Atmos. Chem. Phys.*, **18**, 1003–1022, https://doi.org/10.5194/acp-18-1003-2018.

——, ——, L. R. Leung, and F. Zhang, 2018b: Multiscale atmospheric overturning of the Indian summer monsoon as seen through isentropic analysis. *J. Atmos. Sci.*, **75**, 3011–3030, https://doi.org/10.1175/JAS-D-18-0068.1.

Dallard, T., and G. Spedding, 1993: 2-D wavelet transform: Generalization of the Hardy space and application to experimental studies. *Euro. J. Mech., B/Fluids*, **12**, 107–134, https://cir.nii.ac.jp/crid/1573668926469621376.

Davis, C. A., and M. L. Weisman, 1994: Balanced dynamics of mesoscale vortices produced in simulated convective systems. *J. Atmos. Sci.*, **51**, 2005–2030, https://doi.org/10.1175/1520-0469(1994)051<2005:BDOMVP>2.0.CO;2.

Durran, D. R., and M. Gingrich, 2014: Atmospheric predictability: Why butterflies are not of practical importance. *J. Atmos. Sci.*, **71**, 2476–2488, https://doi.org/10.1175/JAS-D-14-0007.1.

——, and J. A. Weyn, 2016: Thunderstorms do not get butterflies. *Bull. Amer. Meteor. Soc.*, **97**, 237–243, https://doi.org/10.1175/BAMS-D-15-00070.1.

Farge, M., 1992: Wavelet transforms and their applications to turbulence. *Annu. Rev. Fluid Mech.*, **24**, 395–457.

Hamilton, K., Y. O. Takahashi, and W. Ohfuchi, 2008: Mesoscale spectrum of atmospheric motions investigated in a very fine resolution global general circulation model. *J. Geophys. Res.*, **113**, D18110, https://doi.org/10.1029/2008JD009785.

Han, J., and H.-L. Pan, 2011: Revision of convection and vertical diffusion schemes in the NCEP Global Forecast System. *Wea. Forecasting*, **26**, 520–533, https://doi.org/10.1175/WAF-D-10-05038.1.

——, W. Wang, Y. C. Kwon, S.-Y. Hong, V. Tallapragada, and F. Yang, 2017: Updates in the NCEP GFS cumulus convection schemes with scale and aerosol awareness. *Wea. Forecasting*, **32**, 2005–2017, https://doi.org/10.1175/WAF-D-17-0046.1.

Han, Y., P. van Delst, Q. Liu, F. Weng, B. Yan, R. Treadon, and J. Derber, 2006: JCSDA Community Radiative Transfer Model (CRTM)—Version 1. NOAA Tech. Rep. NESDIS 122, 40 pp., https://www.star.nesdis.noaa.gov/pub/smcd/jcsda/qliu/REL_2.1.3_June21_2013/CRTM_v1-NOAA_Tech_Report_NESDIS122.pdf.

——, F. Weng, Q. Liu, and P. van Delst, 2007: A fast radiative transfer model for SSMIS upper atmosphere sounding channels. *J. Geophys. Res.*, **112**, D11121, https://doi.org/10.1029/2006JD008208.

Hazelton, A. T., L. Harris, and S.-J. Lin, 2018: Evaluation of tropical cyclone structure forecasts in a high-resolution version of the multiscale GFDL fvGFS model. *Wea. Forecasting*, **33**, 419–442, https://doi.org/10.1175/WAF-D-17-0140.1.

Heidinger, A. K., C. O'Dell, R. Bennartz, and T. Greenwald, 2006: The successive-order-of-interaction radiative transfer model. Part I: Model development. *J. Appl. Meteor. Climatol.*, **45**, 1388–1402, https://doi.org/10.1175/JAM2387.1.

Iacono, M. J., J. S. Delamere, E. J. Mlawer, M. W. Shephard, S. A. Clough, and W. D. Collins, 2008: Radiative forcing by long-lived greenhouse gases: Calculations with the AER radiative transfer models. *J. Geophys. Res.*, **113**, D13103, https://doi.org/10.1029/2008JD009944.

Jones, T. A., and Coauthors, 2020: Assimilation of *GOES-16* radiances and retrievals into the Warn-on-Forecast System. *Mon. Wea. Rev.*, **148**, 1829–1859, https://doi.org/10.1175/MWR-D-19-0379.1.

Judt, F., 2018: Insights into atmospheric predictability through global convection-permitting model simulations. *J. Atmos. Sci.*, **75**, 1477–1497, https://doi.org/10.1175/JAS-D-17-0343.1.

——, 2020: Atmospheric predictability of the tropics, middle latitudes, and polar regions explored through global storm-resolving simulations. *J. Atmos. Sci.*, **77**, 257–276, https://doi.org/10.1175/JAS-D-19-0116.1.

Kirby, J. F., 2005: Which wavelet best reproduces the Fourier power spectrum? *Comput. Geosci.*, **31**, 846–864, https://doi.org/10.1016/j.cageo.2005.01.014.

Lin, S.-J., 2018: Preliminary evaluation of systematic biases in a FV3-powered global cloud-permitting model. *Fifth ENES HPC Workshop on HPC High-Resolution Weather Climate Modelling*, Lecce, Italy, ESiWACE, 1–22.

Lindborg, E., 1999: Can the atmospheric kinetic energy spectrum be explained by two-dimensional turbulence? *J. Fluid Mech.*, **388**, 259–288, https://doi.org/10.1017/S0022112099004851.

Lorenz, E. N., 1969: The predictability of a flow which possesses many scales of motion. *Tellus*, **21**, 289–307, https://doi.org/10.1111/j.2153-3490.1969.tb00444.x.

Malardel, S., and N. P. Wedi, 2016: How does subgrid-scale parametrization influence nonlinear spectral energy fluxes in global NWP models? *J. Geophys. Res. Atmos.*, **121**, 5395–5410, https://doi.org/10.1002/2015JD023970.

Matsuno, T., 1966: Quasi-geostrophic motions in the equatorial area. *J. Meteor. Soc. Japan Ser. II*, **44**, 25–43, https://doi.org/10.2151/jmsj1965.44.1_25.

Melhauser, C., and F. Zhang, 2012: Practical and intrinsic predictability of severe and convective weather at the mesoscales. *J. Atmos. Sci.*, **69**, 3350–3371, https://doi.org/10.1175/JAS-D-11-0315.1.

Nastrom, G. D., and K. S. Gage, 1985: A climatology of atmospheric wavenumber spectra of wind and temperature observed by commercial aircraft. *J. Atmos. Sci.*, **42**, 950–960, https://doi.org/10.1175/1520-0469(1985)042<0950:ACOAWS>2.0.CO;2.

Schmit, T. J., P. Griffith, M. M. Gunshor, J. M. Daniels, S. J. Goodman, and W. J. Lebair, 2017: A closer look at the ABI on the GOES-R series. *Bull. Amer. Meteor. Soc.*, **98**, 681–698, https://doi.org/10.1175/BAMS-D-15-00230.1.

Selz, T., and G. C. Craig, 2015: Upscale error growth in a high-resolution simulation of a summertime weather event over Europe. *Mon. Wea. Rev.*, **143**, 813–827, https://doi.org/10.1175/MWR-D-14-00140.1.

Shamir, O., C. Schwartz, C. I. Garfinkel, and N. Paldor, 2021: The power distribution between symmetric and anti-symmetric components of the tropical wavenumber–frequency spectrum. *J. Atmos. Sci.*, **78**, 1983–1998, https://doi.org/10.1175/JAS-D-20-0283.1.

Skamarock, W. C., 2004: Evaluating mesoscale NWP models using kinetic energy spectra. *Mon. Wea. Rev.*, **132**, 3019–3032, https://doi.org/10.1175/MWR2830.1.

——, S.-H. Park, J. B. Klemp, and C. Snyder, 2014: Atmospheric kinetic energy spectra from global high-resolution nonhydrostatic simulations. *J. Atmos. Sci.*, **71**, 4369–4381, https://doi.org/10.1175/JAS-D-14-0114.1.

——, C. Snyder, J. B. Klemp, and S.-H. Park, 2019: Vertical resolution requirements in atmospheric simulation. *Mon. Wea. Rev.*, **147**, 2641–2656, https://doi.org/10.1175/MWR-D-19-0043.1.

Sun, Y. Q., and F. Zhang, 2016: Intrinsic versus practical limits of atmospheric predictability and the significance of the butterfly effect. *J. Atmos. Sci.*, **73**, 1419–1438, https://doi.org/10.1175/JAS-D-15-0142.1.

——, R. Rotunno, and F. Zhang, 2017: Contributions of moist convection and internal gravity waves to building the atmospheric −5/3 kinetic energy spectra. *J. Atmos. Sci.*, **74**, 185–201, https://doi.org/10.1175/JAS-D-16-0097.1.

Tennekes, H., and J. L. Lumley, 1972: *A First Course in Turbulence*. The MIT Press, 300 pp.

Terasaki, K., H. L. Tanaka, and M. Satoh, 2009: Characteristics of the kinetic energy spectrum of NICAM model atmosphere. *SOLSA*, **5**, 180–183, https://doi.org/10.2151/sola.2009-046.

Tian, B., I. M. Held, N.-C. Lau, and B. J. Soden, 2005: Diurnal cycle of summertime deep convection over North America: A satellite perspective. *J. Geophys. Res.*, **110**, D08108, https://doi.org/10.1029/2004JD005275.

Waite, M. L., and C. Snyder, 2009: The mesoscale kinetic energy spectrum of a baroclinic life cycle. *J. Atmos. Sci.*, **66**, 883–901, https://doi.org/10.1175/2008JAS2829.1.

——, and ——, 2013: Mesoscale energy spectra of moist baroclinic waves. *J. Atmos. Sci.*, **70**, 1242–1256, https://doi.org/10.1175/JAS-D-11-0347.1.

Weisman, M. L., W. C. Skamarock, and J. B. Klemp, 1997: The resolution dependence of explicitly modeled convective systems. *Mon. Wea. Rev.*, **125**, 527–548, https://doi.org/10.1175/1520-0493(1997)125<0527:TRDOEM>2.0.CO;2.

Zhang, F., C. Snyder, and R. Rotunno, 2003: Effects of moist convection on mesoscale predictability. *J. Atmos. Sci.*, **60**, 1173–1185, https://doi.org/10.1175/1520-0469(2003)060<1173:EOMCOM>2.0.CO;2.

——, N. Bei, R. Rotunno, C. Snyder, and C. C. Epifanio, 2007: Mesoscale predictability of moist baroclinic waves: Convection-permitting experiments and multistage error growth dynamics. *J. Atmos. Sci.*, **64**, 3579–3594, https://doi.org/10.1175/JAS4028.1.

——, M. Minamide, R. G. Nystrom, X. Chen, S.-J. Lin, and L. M. Harris, 2019: Improving Harvey forecasts with next-generation weather satellites: Advanced hurricane analysis and prediction with assimilation of GOES-R all-sky radiances. *Bull. Amer. Meteor. Soc.*, **100**, 1217–1222, https://doi.org/10.1175/BAMS-D-18-0149.1.

Zhao, Q., and F. H. Carr, 1997: A prognostic cloud scheme for operational NWP models. *Mon. Wea. Rev.*, **125**, 1931–1953, https://doi.org/10.1175/1520-0493(1997)125<1931:APCSFO>2.0.CO;2.

Zhou, L., S.-J. Lin, J.-H. Chen, L. M. Harris, X. Chen, and S. L. Rees, 2019: Toward convective-scale prediction within the next generation global prediction system. *Bull. Amer. Meteor. Soc.*, **100**, 1225–1243, https://doi.org/10.1175/BAMS-D-17-0246.1.